Advanced Fiber Materials (2020) 2:93–104
https://doi.org/10.1007/s42765-020-00029-9

RESEARCH ARTICLE

Coupling of Hierarchical Al_2O_3/TiO_2 Nanofibers into 3D Photothermal Aerogels Toward Simultaneous Water Evaporation and Purification

Xiangyu Meng[1] · Wanlin Xu[1] · Zhihui Li[1] · Jianhui Yang[1] · Jingwu Zhao[1] · Xixi Zou[1] · Yueming Sun[1] · Yunqian Dai[1]

Received: 13 December 2019 / Accepted: 23 January 2020 / Published online: 11 February 2020

Abstract

Serious freshwater shortage and environmental pollution boost the rapid development of solar-driven water production. Although improved evaporation rate has achieved in recent years, undesirable impurity (e.g., pollutant components) can also be inevitably evaporated and collected as impurity in produced freshwater. This work reports new ultra-light three-dimensional (3D) aerogels assembled by hierarchical Al_2O_3/TiO_2 nanofibers and reduced graphene oxide (RGO) for exciting synchronized solar-driven evaporation and water purification. Hydrophilic Al_2O_3/TiO_2 fibrous channels linked up the graphene hot-spots and water body for sufficient water supply and bulk water insulation. Meanwhile, featured with thermal insulation effect, the Al_2O_3/TiO_2 nanofibers effectively locked the converted heat with less energy loss from sunlight. The introducing of Al_2O_3/TiO_2 nanofibers into RGO aerogel led to the effective interfacial evaporation for a more rapid water evaporation rate ($2.19\ \mathrm{kg \cdot m^{-2} \cdot h^{-1}}$, normalized to evaporation area including both top and side surface), which was 36% higher than that of pristine RGO aerogel. Moreover, simultaneous with the strong steam generation, Al_2O_3/TiO_2 nanofibers in situ removed the pollutants within steam by photodegradation, achieving polluted wastewater purification with high contaminant removal ratio of 91.3%. Our work on coupling Al_2O_3/TiO_2 nanofibers into photothermal aerogel provides attractive solutions for the challenges of clean water scarcity and serious environmental pollution.

Keywords Graphene · Nanofiber · Aerogel · Solar · Photocatalysis

Introduction

The clean and fresh water scarcity is now becoming a critical global issue. Traditional water treatment mainly based on water desalination, reverse osmosis, electro-dialysis membrane distillation, and so on [1–3]. Most of these approaches are still accompanied by high energy consumption and greatly accelerate greenhouse gas emissions. To meet the urgent demand of water, solar energy is an attractive renewable-energy resource and can be directly used for water production. Recently, solar-driven water evaporation has emerged as a new and promising technology for producing fresh water through a sustainable and low-cost approach. Nevertheless, undesirable impurity (e.g., organic dyes) in water can also be inevitably evaporated associated with vapor and thus be collected in the evaporated water [4], which is significantly harmful to public health and human body. Hence, coupling effective water purification with water evaporation for directly harvesting clean water from contaminated water (e.g., sewage) is very significant [5–7]. Semiconductors (e.g., TiO_2, Al_2O_3) can effectively utilize sunlight to photodegrade organic molecules into nontoxic products [8]. Especially, electrospun nanofibers based on semiconductors can endow with large surface area, enriched pores, and unique one-dimensional (1D) architectures [9, 10]. These unique attributes enable semiconductor nanofibers to serve as superior photocatalysts. However, toward solar steam generation, their poor photothermal conversion capabilities significantly hinder their uses as effective solar evaporators. Coupling semiconductor nanofibers into new photothermal materials can overcome this disadvantage and lead to the exciting performance in both solar-driven evaporation and water purification.

Electronic supplementary material The online version of this article (https://doi.org/10.1007/s42765-020-00029-9) contains supplementary material, which is available to authorized users.

✉ Yunqian Dai
daiy@seu.edu.cn

[1] School of Chemistry and Chemical Engineering, Southeast University, Nanjing, Jiangsu 211189, People's Republic of China

Graphene and their derivatives have recently emerged as most promising photothermal materials toward solar water evaporation, as they are commonly featured with good light harvesting, excellent light-to-heat conversion and tunable thermal conductivity [11]. Assembling two-dimensional (2D) graphene-based sheets into three-dimensional (3D) aerogel can further enhance the solar utilization by the multiple light-matter interactions and by recovering most diffuse reflected light through the adsorption of 3D walls [12]. However, the inherent poor water wettability, reduced surface area caused by irreversible re-stacking of neighboring sheets, and undesirable heat loss severely hamper the strong steam-generating in the conventional graphene aerogel [13]. Besides, although the graphene aerogel can somehow capture contamination in liquid water and/or steam by physiochemical adsorption, the pollutants can accumulate on the graphene surface and thus inevitably cause light-blocking and evaporation-area lose [14]. It is also worth pointing out the interconnected pores within most aerogels can lead to circuitous routes for water transfer and unsatisfied performance in solar steam generation. In sharp contrast, straight channels can offer direct pathways and thus enable rapid vapor release in a short route. Therefore, constructing straight channels into aerogels can endow resultant graphene aerogels with enhanced water/vapor transfer by wicking effect toward solar vapor generation.

Herein, we simply introduced hierarchical Al_2O_3/TiO_2 nanofibers into 3D graphene aerogel with hydrophilicity, good thermal insulation and photocatalytic ability in the aim of achieving water evaporation and purification simultaneously. As illustration in Scheme 1, compared with traditional graphene aerogels, the unique semiconductor nanofibers within new aerogels can play three key roles: (1) offering direct and hydrophilic channels within 3D aerogel toward enhanced water transfer by wicking effect; (2) providing photocatalytic sites that can enable residual pollutants to be in situ photodegraded under solar irradiation; (3) serving as reliable skeletons to effectively prevent the irreversible aggregation of graphene sheets in the lightweight 3D aerogels.

Experimental Section

Materials

Graphite powder (99.95%, 325 meshes) was obtained from XFNANO Tech. Co., Ltd. Polyvinylpyrrolidone (PVP, $M_w \approx 1.3 \times 10^6$), titanium isopropoxide (TTIP) and aluminum acetylacetonate ($Al(acac)_3$) were purchased from the Alfa Aesar. Acetic acid and other chemicals were gotten from the Sinopharm Chemical Reagent Co., Ltd. The water used in all experiments was filtered through a Millipore filtration system with a resistivity of 18.2 MΩ · cm.

Fabrication of Electrospun Al_2O_3/TiO_2 Nanofibers

The Al_2O_3/TiO_2 nanofibers were obtained by electrospinning the homogeneous precursor containing 0.45 g of PVP, 4.5 mL of ethanol, 1 g of $Al(acac)_3$, 5 mL of acetone, 1.43 mL of TTIP and 3 mL of acetic acid after magnetic stirring for 12 h. The flow rate was 0.5 $mL \cdot h^{-1}$, the vertical distance from needle to grounded aluminum foil (collector) was 12.5 cm and the applied voltage was 18 kV. The as-spun nanofibers were calcined at 600 °C for 2 h in air, with a ramping rate of 2.7 $°C \cdot min^{-1}$.

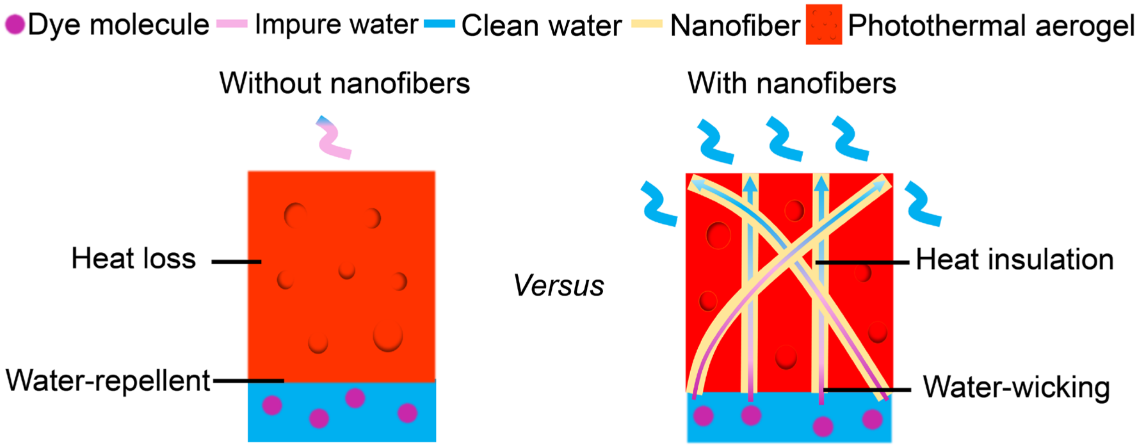

Scheme 1 The enhancement of solar-driven water evaporation and purification performance of dye-containing wastewater by introducing Al_2O_3/TiO_2 nanofibers into photothermal aerogels

Fabrication of Al_2O_3/TiO_2/RGO Aerogels

Graphene oxide (GO) was prepared from a modified Hummers method [15]. The Al_2O_3/TiO_2 nanofibers were well dispersed in water with the concentration of 3, 6, 12 $mg \cdot mL^{-1}$, then the nanofiber suspension was added into the GO aqueous solution (3 $mg \cdot mL^{-1}$) (named as AT-1/RGO, AT-2/RGO and AT-4/RGO) to obtain the reaction precursor with different mass ratio between Al_2O_3/TiO_2 and RGO. Then, the uniformly mixed solution was hydrothermally reacted at 180 °C for 8 h in the 25 mL autoclave. The resultant hydrogels were frozen in refrigerator (DW-86L626, Haier) under controlled temperatures followed by freeze-drying under − 50 °C for 8 h in freeze-drier (FD-1A-50, Jiangsu Tianlin Instrument Co., Ltd.). To show the intact profile of AT-4/RGO aerogel, the sample was prepared under the same conditions but in a 5 mL autoclave.

Measurement of Density and Porosity of Aerogel

The weight of aerogel was tested by a XPR ultra-microbalance (Mettler Toledo) with accuracy down to 0.1 µg. The volume of aerogel was calculated by the cylindrical model. The porosity was tested by Mercury porosimeter (AutoPore IV 9500, Micromeritics). Before testing, the aerogel was pre-dried at 105 °C for 1 h, and outgassed at ambient temperature for another 1 h. Meanwhile, the bulk density of aerogel was further confirmed by the results from AutoPore IV 9500.

Measurement of Thermal Conductivities and Photothermal Conversion Efficiencies

The thermal conductivities (λ) were tested by a heat flow meter (HFM 446 Lambda, Netzsch) and calculated through the Eq. (1) [16]:

$$\lambda = \alpha \cdot Cp \cdot \rho \tag{1}$$

where α is the thermal diffusivity ($m^2 \cdot s^{-1}$), Cp is the specific heat capacity ($J \cdot g^{-1} \cdot K^{-1}$), and ρ is the density ($g \cdot cm^{-3}$).

The photothermal conversion efficiency was calculated from the temperature data on infrared images taken by an infrared camera (Ti9, Fluke). When the temperature remained stable, the heat converted from light was regarded as equal to the thermal dissipation between the irradiation surface of sample and the environment. Hence, the photothermal conversion efficiency (E) can be calculated by Eq. (2) [17]:

$$E = \frac{h \cdot A \cdot (T_{\mathrm{after}} - T_{\mathrm{before}})}{\rho_{\mathrm{L}} \cdot A} \tag{2}$$

where h is the convection heat transfer coefficient ($W \cdot m^{-2} \cdot K^{-1}$), A is the exposed surface area including the top surface and sidewall surface of the cylindrical aerogels (m^2), T_{before} and T_{after} are the temperatures of aerogel before and after light irradiation (2 $kW \cdot m^{-2}$) for 1 h (K), respectively. ρ_{L} is the light power density ($W \cdot m^{-2}$).

Measurement of Water Evaporation Performance

The aerogel was cut into cylinder with the height of 5 mm and then set on the water contained by a flat mouth beaker. To eliminate the extra irradiation surface of water, a polyethylene foam was covered between the aerogel sidewall and beaker sidewall. Then, the steam generation was tested under the light irradiation from Xenon lamp (CEL-HXF300, Beijing Aulight Co., Ltd.), while the water mass change was measured by an electronic microbalance (XP26, Mettler Toledo).

Estimation of the Performance of Water Purification

The photocatalytic performance of aerogel was evaluated by purifying Rhodamine B (RhB) aqueous solution under light illumination (2 $kW \cdot m^{-2}$). The feed solution (RhB) and the purified solution were collected for UV–Vis spectra testing, respectively. The absorbance of characteristic peak was used to determinate the concentration of RhB, and the dye removal ratio (R_{d}) was calculated by the Eq. (3) [18]:

$$R_{\mathrm{d}} = \left(1 - \frac{C}{C_0}\right) \times 100\% \tag{3}$$

where C_0 is the initial concentration of RhB aqueous solution, C is the concentration of collected solution after the degradation. Since the existence of evaporation in the purification process, the concentration of RhB was calculated based on the considering of mass loss. The pH values of RhB aqueous solution were adjusted by adding different volumes of 1 M HCl or NaOH, and were measured by a pH meter (PHS-3C).

Characterizations

The Raman spectra were obtained from the Raman microscope (DXR2, Thermo Fisher Scientific) with the laser of 532 nm. The field-emission scanning electron microscopy (SEM) image was obtained by Inspect F50 (FEI). Contact angles of the aerogels were collected by the contact angle instrument (OCA 15 plus, Dataphysics).

Results and Discussion

Facile Assembling of Al_2O_3/TiO_2/RGO Aerogels

The composite Al(acac)$_3$/TTIP/PVP nanofibers were simply fabricated by electrospinning a homogeneous solution containing Al(acac)$_3$, TTIP, PVP and solvents. Upon calcination in air at 600 °C, the composite nanofibers were converted into porous, hierarchical Al_2O_3/TiO_2 nanofibers by selectively removing PVP matrix. Then, these nanofibers were mixed with graphene oxide (GO) sheets together and simply assembled into 3D Al_2O_3/TiO_2/RGO aerogels by a hydrothermal reaction followed by freeze-drying (as shown in Fig. 1 and Fig. S1). Commonly, graphene sheets preferred to self-assembling together via re-stacking to reduce their surface energy in the absence of any nanofiber as skeleton (Fig. 1a). At the same time, the GO reduced to RGO and the hydrophilicity decreased significantly. During this process, water and hydrophilic materials could be easily repelled out of RGO hydrogels. When the hydrophilic Al_2O_3/TiO_2 nanofibers were introduced in a low concentration, they were pushed to the outer surface in the resultant aerogels (Fig. 1b) and were disabled to serve as reliable skeleton. In the presence of enough Al_2O_3/TiO_2 nanofibers, the re-stacking of RGO sheets could be hampered by the robust Al_2O_3/TiO_2 nanofibers. Besides, in order to reduce surface energy, the RGO sheets preferred to wrapping and/or rolling outside of the nanofibers instead of re-stacking together, as highlighted by white arrows in Fig. 1c. These observations revealed that the robust nanofibers had great impact on the assembling manner of 2D graphene sheets into 3D aerogels and prevented the irreversible aggregation of graphene by serving as robust skeletons.

The introducing of nanofibers also led to the appearance of exciting hierarchical pore structures in aerogels with ultra-light weight (Fig. 1b, c). Taken AT-4/RGO as one example, Al_2O_3/TiO_2/RGO wrapped around ice crystals to form a honeycomb-like porous network structure during the freeze-drying process, generating macropores ranged from 9 to 52 µm (Fig. S2). Besides, small macropores around 3 µm could be constructed among the crossing of neighboring nanofibers (Fig. 1c). The resultant AT-4/RGO aerogel possessed porosity as high as 90.4%. These hierarchical pores and channels within the aerogel can enhance the multiple interactions between light and matter, improve heat insulation, and provide the favorable capillary force for pumping water from bulky water. These attributes are essential for highly efficient solar energy utilization and continuous water supply upon steam-generation.

Raman spectroscopy is used to verify and characterize the intrinsic structure of the Al_2O_3/TiO_2/RGO aerogels (Fig. 2). The Raman shift at ~ 147 cm^{-1}, ~ 515 cm^{-1}, and ~ 637 cm^{-1} are ascribed to anatase TiO_2, ~ 415 cm^{-1} to the α-Al_2O_3, as well as the D and G band at ~ 1348 cm^{-1} and ~ 1595 cm^{-1} of RGO [19]. These characteristic peaks further confirmed the simultaneous existence of Al_2O_3/TiO_2 nanofibers and RGO, as well as no detectable impurity in the Al_2O_3/TiO_2/RGO aerogel. The resonance of abundant sp^2 structures within RGO wrapped on Al_2O_3/TiO_2 nanofibers can greatly enhance the visible light utilization of TiO_2. Also, the RGO integrated on Al_2O_3/TiO_2 nanofibers can greatly depress the electron combination on TiO_2, and thus leave more charge carriers to evolve into reactive species for effective pollutant-degradation [20]. The increasing ratio of peak intensity at the D band and G band (I_D/I_G) indicated the slight increase of defects of RGO after reduction, which was attributed to the mild fragmentation of RGO sheets along the active sites

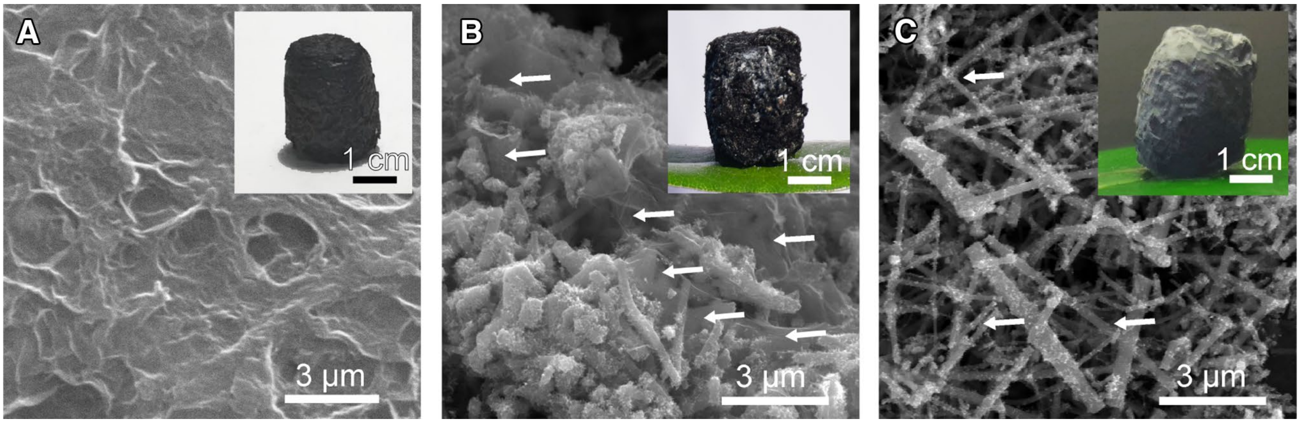

Fig. 1 **a** The SEM image of pristine RGO aerogel. **b** SEM image of Al_2O_3/TiO_2/RGO fibrous aerogel fabricated with the fibers concentration of 50 wt%, showing the small amounts of aggregative fibers and a large amounts of RGO. **C** SEM image of aerogel fabricated with the fibers concentration of 80 wt%, showing uniform fibrous frameworks and thin RGO films. The insets show the corresponding optical images of the lightweight aerogels

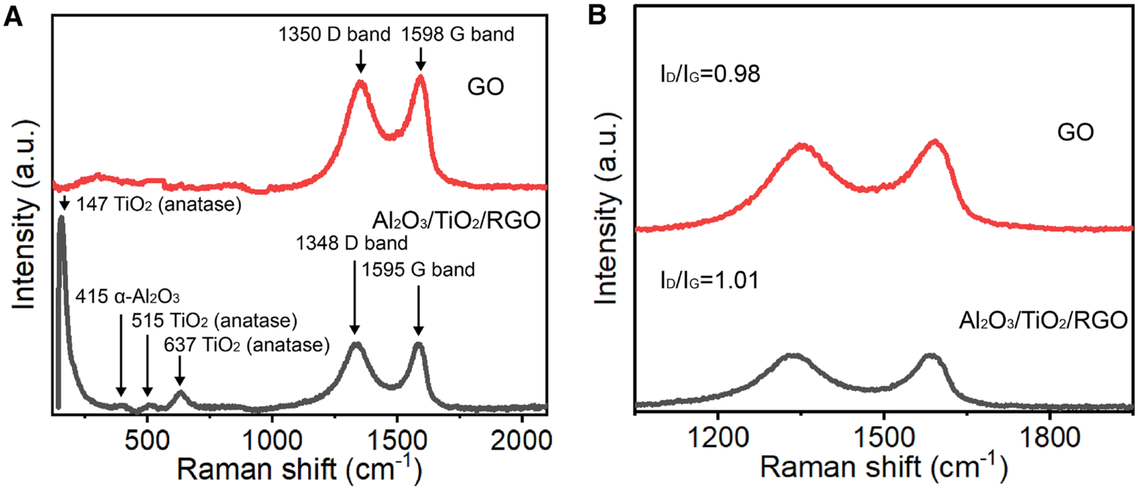

Fig. 2 **a** The Raman spectra of GO and Al_2O_3/TiO_2/RGO fibrous aerogel. **b** The D and G bands of GO and RGO

and thus the appearance of new edges after hydrothermal reduction [15]. The rising of defects can greatly increase the adsorption sites within RGO sheets to capture more pollutants and facilitate the photodegradation by nanofibers.

Impact of Al_2O_3/TiO_2 Nanofibers on the Density, Thermal Insulation and Hydrophilicity of Aerogels

Representative physical properties of Al_2O_3/TiO_2/RGO aerogels can be simply tuned by the weight ratio of nanofibers within aerogels. It should be noted that the density of aerogel drastically decreased from 0.17 to 0.08 $g \cdot cm^{-3}$ with the increasing nanofibers (Fig. 3a), which was attributed to the abundant hierarchical pores introduced by crossing nanofibers, as well as the rising volume enlarged by hampering of self-stacking among RGO sheets. Meanwhile, the wall thickness of individual RGO within aerogel sharply decreased due to the less re-stacking within Al_2O_3/TiO_2/RGO aerogel (Fig. 3b, c). The wall thickness of RGO strikingly decreased from 852.9 to 54.9 nm after introducing Al_2O_3/TiO_2 nanofibers into RGO aerogels. Thinner RGO wall with less layer-numbers can conduct thermal phonons more rapidly (Fig. 3c) [21], due to the reduced resistance of heat transfer between the interfaces of neighboring RGO layers. To further investigate the influence of nanofibers on the thermal management of aerogels, Figs. 3d and 4a recorded the photothermal conversion evolution with the increasing nanofibers based on the infrared images. It can be clearly seen that, compared with pristine RGO aerogel (42.3%), the photothermal conversion efficiency of aerogel decreased at a nanofiber content of 50 wt% (AT-1/RGO) (40.7%), while increased at a larger nanofiber content of 80 wt% (AT-4/RGO) (48.2%). For AT-1/RGO, the nanofibers could somehow decrease the light-harvest area and thus hinder the light-to-heat conversion efficiency. In contrast, for AT-4/RGO aerogel, the fibrous skeletons could hamper the re-stacking of RGO sheets, and thus lead to the enlarged light harvest area and the enhanced thermal conduction of RGO hot spots. Besides, the nanofibers featured with low thermal conductivity could endow the whole new aerogels with decreased thermal conductivity from 0.91 to as low as 0.16 $W \cdot m^{-1} \cdot K^{-1}$ (Table S1), and thus provide a good heat-insulation effect. As a result, compared to recent works [22–24], our new aerogels achieved satisfactory photothermal conversion (48.2%) despite less amount of photothermal materials were employed.

Besides, the water wetting ability of aerogel was also strikingly enhanced by the hydrophilic ceramic nanofibers, which was confirmed by the water contact angles in Fig. 4b. The super-hydrophilic performance of Al_2O_3/TiO_2 nanofibers can be attributed to their favorable hierarchical and hetero-structures, which can powerfully draw water toward nanofibers by capillary forces [25]. These interconnected nanofibers with superb wettability formed abundant 1D channels for rapid and continuous water wicking from bulky water. Meanwhile, the hierarchical pores constructed by RGO network and crossing gaps among nanofibers could further accelerate the water pumping within aerogel.

Water Evaporation Performance of Al_2O_3/TiO_2/RGO Aerogels

The water mass changes of aerogels *versus* time under light irradiation were recorded to estimate the kinetics of water evaporation (Fig. 5a). The corresponding evaporation rates were calculated from mass changes, which had been subtracted by the amount of water evaporation under dark evaporation. The equilibrium temperatures of aerogels and pure water were also summarized in Fig. 5b. It should be noted that the evaporation rate of AT-4/RGO (2.19 $kg \cdot m^{-2} \cdot h^{-1}$)

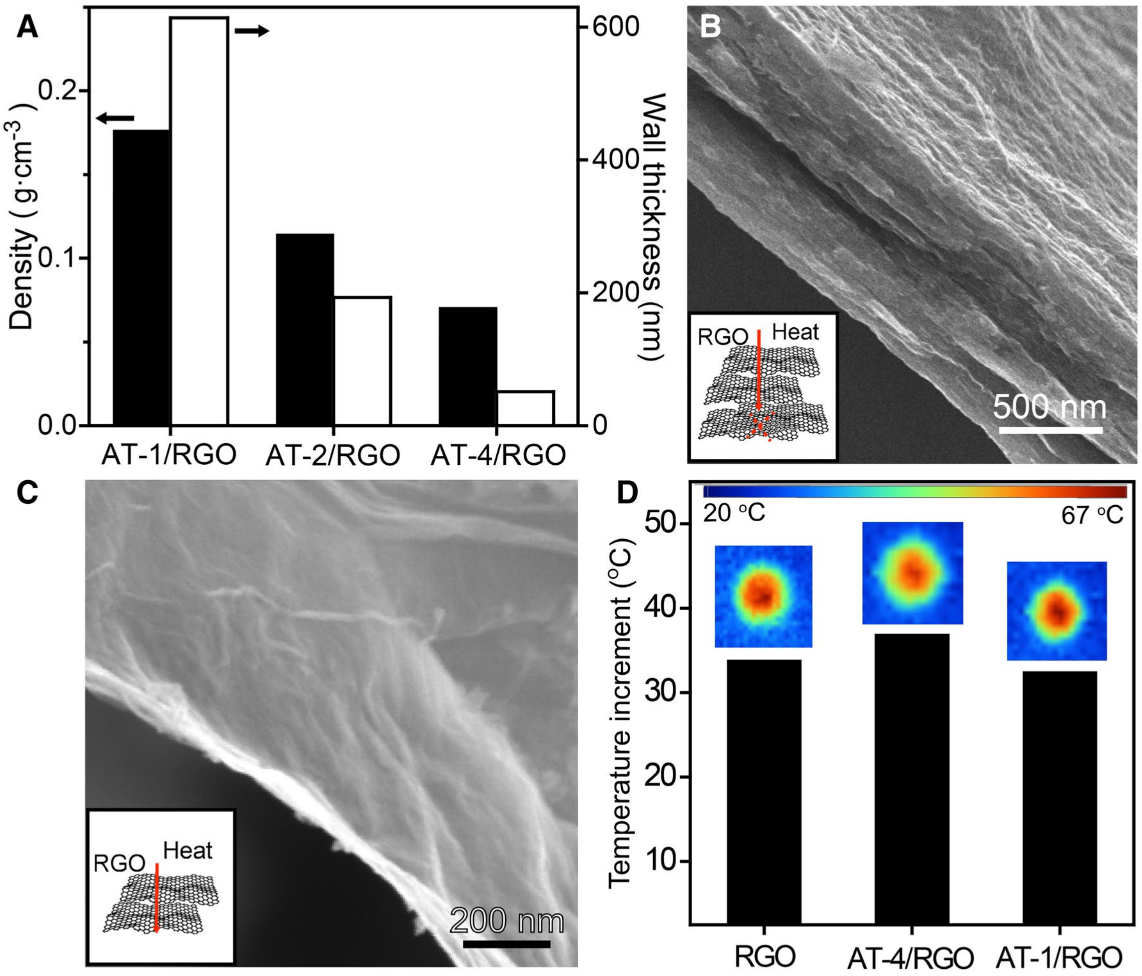

Fig. 3 **a** The densities of aerogels (black bar) and wall thicknesses of RGO walls (white bar) with the increasing amounts of Al_2O_3/TiO_2 nanofibers. The SEM of RGO walls **b** in pristine RGO and **c** in AT-4/RGO, the decreased wall thickness is beneficial to the rapid heat conduction (insets). **d** The temperature increment of aerogels after light irradiation (2 $kW \cdot m^{-2}$) for one hour, the insets are corresponding infrared images

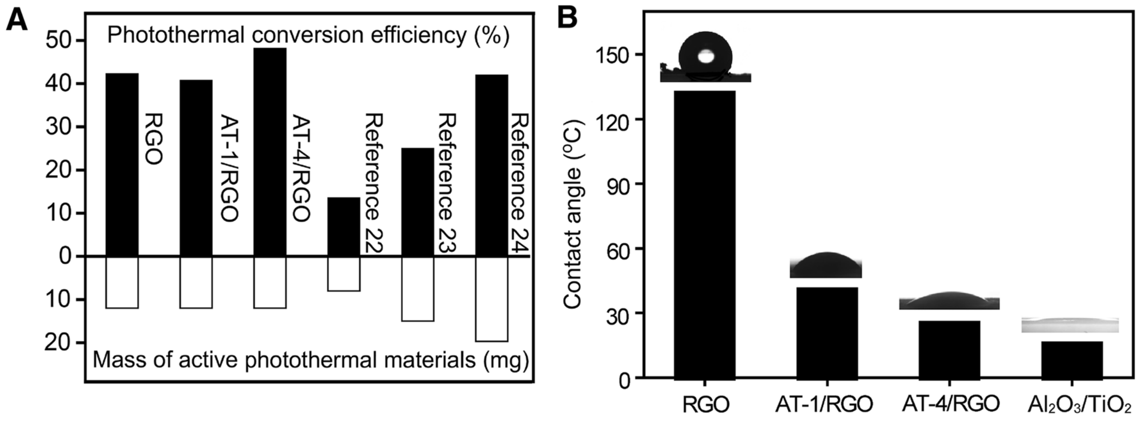

Fig. 4 **a** The photothermal conversion efficiency under light irradiation and the corresponding mass of photothermal material. Data were given in the Refs. [22–24]. **b** The wettability of aerogels and hierarchial Al_2O_3/TiO_2 nanofibers

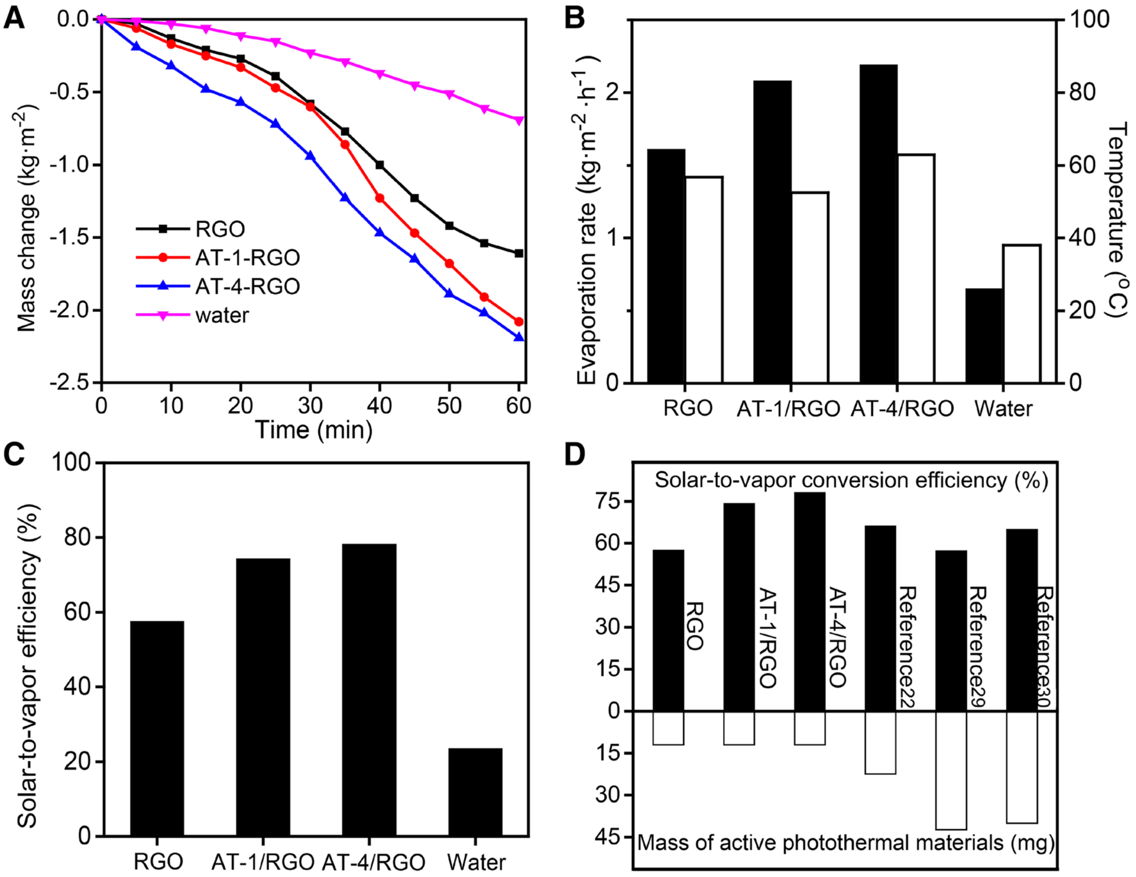

Fig. 5 **a** The mass change, **b** (black bar) evaporation rate, (white bar) temperature, and **c** corresponding solar-to-vapor efficiency of aerogels and water. **d** Comparison of the photothermal conversion efficiency and the corresponding mass of photothermal materials. Data were given in the respective Refs. [22, 29, 30]

was much higher than others, which was 36% higher than that of the conventional RGO (1.61 $\mathrm{kg \cdot m^{-2} \cdot h^{-1}}$). Such a large enhancement on evaporation by introducing nanofibers was attributed to three reasons as followings: (1) the hydrophilic nanofibers served as 1D channels for providing rapid and continuous water wicking from bulky water; (2) the local water supply from nanofiber to hot spot on RGO led to the effective in situ interfacial water evaporation; [26, 27] (3) the fibrous frameworks enhanced both light utilization and thermal insulation of photothermal aerogels.

Solar-to-vapor conversion efficiency (η) (Fig. 5c) was calculated based on evaporation rate and the Eq. (4) [28]:

$$\eta = \frac{m \cdot h_{LV}}{\rho_L} \tag{4}$$

where m is the water evaporation rate ($\mathrm{kg \cdot m^{-2} \cdot h^{-1}}$), h_{LV} is the total enthalpy of water–vapor phase conversion, including sensible heat and phase conversion enthalpy ($\mathrm{J \cdot kg^{-1}}$), and ρ_{L} is the light power density ($\mathrm{W \cdot m^{-2}}$). The η of AT-4/RGO was as high as 78.2%, while the η of conventional RGO and pure water was only 57.5% and 23.5%, respectively. Notably, compared to the recent works, the solar-to-vapor conversion performance of Al_2O_3/TiO_2/RGO aerogels showed less dependence on photothermal materials (Fig. 5d) [22, 29, 30]. Also, the evaporation rates showed a liner growth as the enhancement of light-intensity (Fig. S3), indicating that manipulation solar-driven water evaporation of Al_2O_3/TiO_2/RGO aerogel can be simply achieved by adjusting light-intensity to meet practical demands.

Moreover, the mechanical robustness of evaporator was critical for practical usage. Hence, mechanical property of Al_2O_3/TiO_2/RGO aerogel (AT-4/RGO) was also carefully tested. Figure S4 shows compressive stress–strain curve of AT-4/RGO aerogel under a large strain of 50%. The aerogel can withstand external compressive stress over its own weight, and endow with maximum stress of 3.89 kPa, Young's modulus of 7.29 kPa as well as a low energy loss coefficient of 0.22. These favorable features of AT-4/RGO aerogel in mechanical strength and large deformation endow them with ability to work under harsh environmental conditions such as strong sea waves, wind and rain.

Solar-Driven Water Purification of $Al_2O_3/TiO_2/RGO$ Aerogels

Dye-containing wastewaters which mainly from textile and paper industries, are considered as a wide variety of organic pollutants introduced into the natural water resources [31]. Hence, Rhodamine B (RhB) ($1.5\ g \cdot L^{-1}$) and Congo red (CR) ($1\ g \cdot L^{-1}$) solution were chosen as the simulated polluted wastewater models to estimate the water purification performance of our aerogels. After setting the $Al_2O_3/TiO_2/$ RGO aerogel (AT-4/RGO) on the simulated polluted water surface under dark at the room temperature for 1 h to reach the adsorption–desorption equilibrium, the aerogel harvested light and generated steam which would be condensed and collected in a home-made set-up (Fig. 6a). The aforementioned satisfying solar-driven steam generation can offer the strong enough driving force for carrying contaminations out of the polluted water through $Al_2O_3/TiO_2/RGO$ aerogel in an anti-gravity way. The resultant collected water is colorless and transparent, in sharp contrast to the feeding water (Fig. 6b). UV–Vis spectra in Fig. 6c were used to test the concentration of pollutants in sewage and the purified water. It can be clearly seen that the RhB and CR feed solutions presented characteristic adsorption peaks at around 553 nm (RhB), 350 nm (CR), and 490 nm (CR), respectively [6], while no obvious detectable peak was characterized for the steamed water.

To investigate the contributions of photodegradation on purification performance of $Al_2O_3/TiO_2/RGO$ aerogel, the aerogels were immersed in simulated polluted water under dark and light irradiation for 1 h, respectively. The increase in concentration of pollutant in simulated dye-containing wastewater caused by water evaporation was considered in the calculations. It should be noted that the removal ratio of RhB in sewage under light-irradiation was as high as 91.3%, which was almost 1.68 times higher than that of under dark

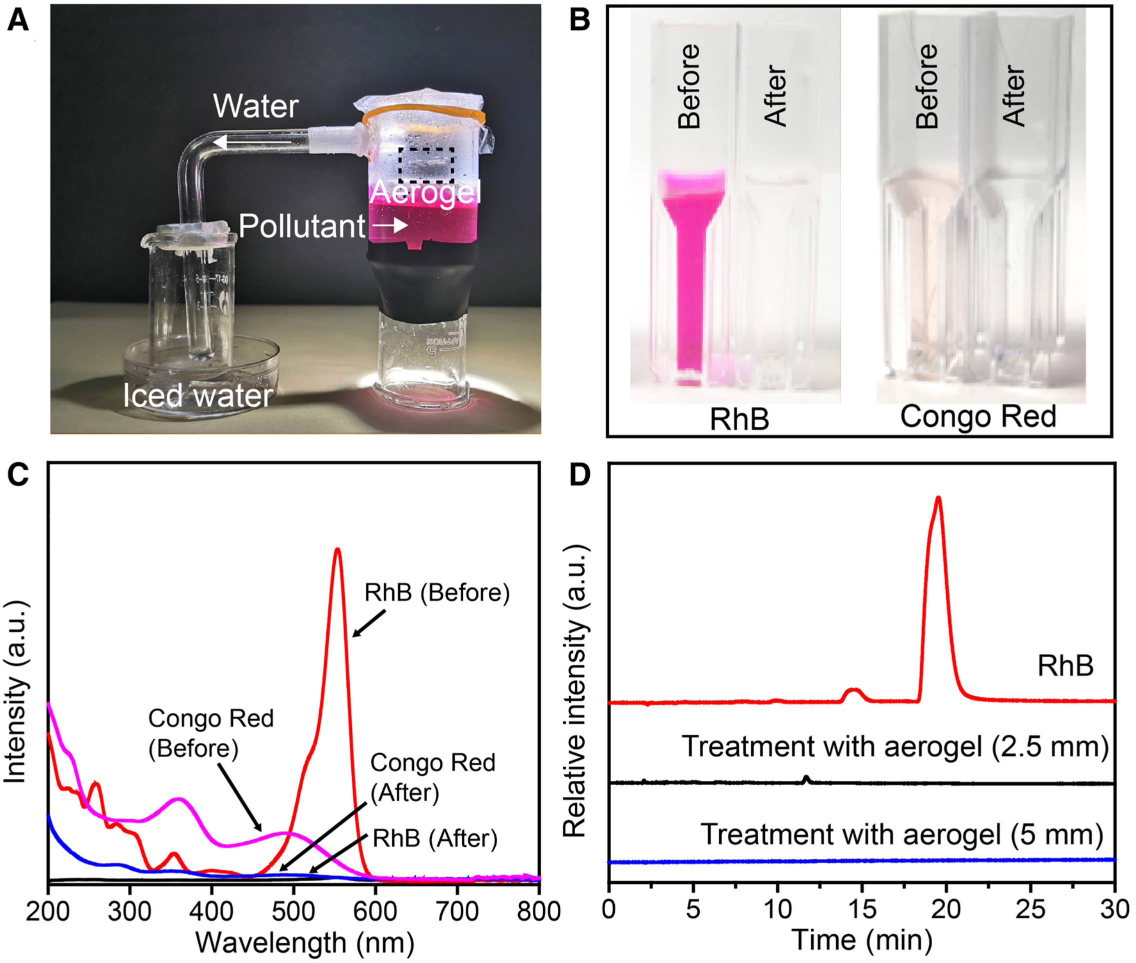

Fig. 6 **a** The optical image of the experimental setup. **b** The optical images of water before and after purification. **c** The UV–Vis spectra of collected water before and after purification by $Al_2O_3/TiO_2/RGO$ (AT-4/RGO) aerogel. **d** The high-performance liquid chromatography spectra of collected water purified by $Al_2O_3/TiO_2/RGO$ (AT-4/RGO) aerogels with the height of 2.5 mm and 5 mm, respectively

(54.2%), indicating the presence of effective photodegradation (Fig. S5). Commonly, the physical and/or chemical adsorption can remove pollutants from sewage without generating any harmful by-product, and is stable at any level of light intensity. Therefore, our Al_2O_3/TiO_2/RGO aerogel with both adsorption and photodegradation functions can overcome the limitations of two individual methods, and remove pollutants completely, thus provide an optimized system for fresh, clean water supplying in all climates. To further simulate the water purification performance even if under lower intensity of solar irradiation, the collected steaming water from aerogel under 1 sun was characterized by UV–Vis spectra (Fig. S6). As expected, high dye removal ratios were also observed for both Congo red (91.7%) and Rhodamine B (90.0%) simulated sewage, indicating the satisfying performance under flexible working conditions.

Besides, the degradation products purified by the Al_2O_3/TiO_2/RGO aerogels with different heights were tested by the high-performance liquid chromatography (HPLC) (Fig. 6d) and mass spectra (Fig. 7) to further understand the photodegradation pathway of RhB. As expected, the collected water purified by aerogel with the height of 5 mm mainly involved small molecules of oxygen-containing compounds, such as ethane-1,2-diol, and trace amounts of dibutyl phthalate (DBP) with concentration far below 10 ppm (calculated from high-performance liquid chromatography in Fig. S7), which are nontoxic and can be further refined into fuel. In contrast, the water treated by aerogel with half of the pristine aerogel height (2.5 mm) retained a few intermediate products, which were confirmed by HPLC spectra and highlighted in the mass spectra [32, 33]. On one hand, these intermediate products indicated that two competitive processes occurred simultaneously during the photoreaction: N-demethylation and destruction of dye chromophore structures. On the other hand, the 3D fibrous channels effectively elongated the water treatment route of adsorption and photodegradation, thus strikingly reduced the residue of polluted compounds compared to conventional photocatalytic materials based on 2D membranes.

Since pH value plays a key role in RhB degradation in real-world working conditions, the water purifications under simulated alkaline solution (pH = 8.9), neutral water (pH = 7) and acidic solution (pH = 2.8 and 5.6) were conducted, respectively. Considering the high removal ratio of RhB achieved by aerogels with heights of 5 mm, the aerogels with half heights (2.5 mm) were used for more clearly illustrating pH effect. From the results in Fig. S8, it can be seen that the dye removal ratio of RhB gradually increased with the arising of pH values. In acidic solution, the surface of Al_2O_3/TiO_2/RGO was positively charged and provided less adsorbing to positively charged RhB molecules. Because the surface of catalysts was negatively charged and RhB was in a zwitterionic form in the alkaline solution, considerable RhB molecules could easily attract on Al_2O_3/TiO_2/RGO surface. Moreover, more hydroxide ions on catalysts' surface could be transferred into active •OH in alkaline solution, thus the efficiency of the photocatalytic process was further enhanced [34]. Endowed with favorable environmental adaptation with rather stable purification on a broad range of pH values, our aerogel is promising for actual water purification. To further investigate the stability of our aerogels, cycling tests were conducted under continuous purification of simulated RhB sewage for 6 h. Notably, the dye removal ratio still maintained over 89%, which was 97.5% of initial removal

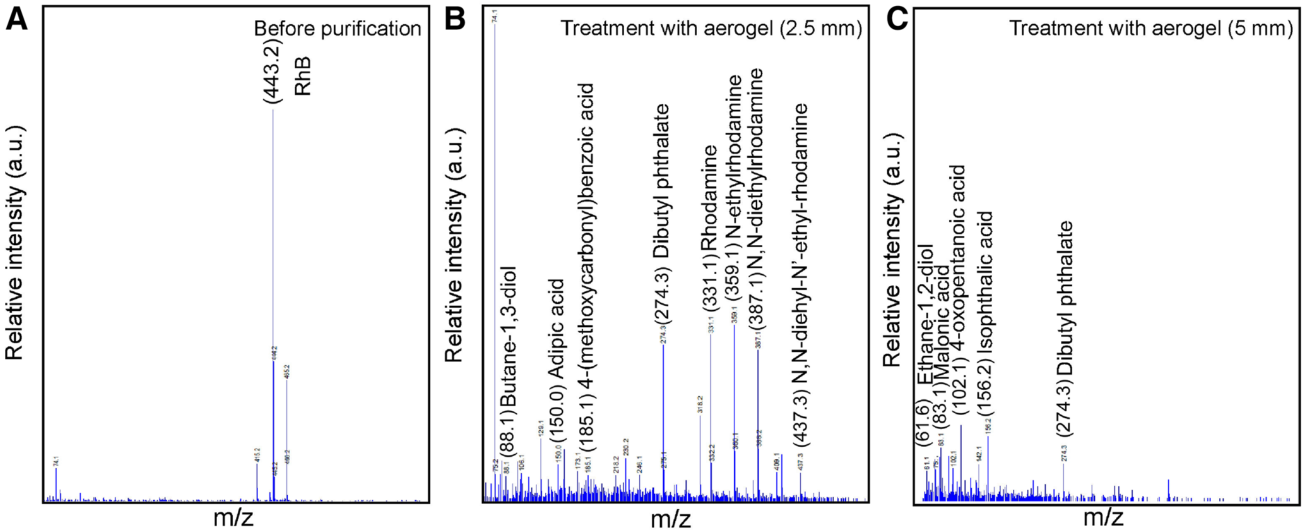

Fig. 7 The mass spectra of **a** the pollutant water before purification, after treatment by Al_2O_3/TiO_2/RGO (AT-4/RGO) aerogels with the height of **b** 2.5 mm and **c** 5 mm

ratio of RhB and attributed to the suppressed dye blocking by rapid photodegradation as well as favorable stability of RGO sheets (Fig. S9).

Conclusion

In conclusion, the Al_2O_3/TiO_2 nanofibers with hierarchical structures were facilely assembled into a 3D ultra-light Al_2O_3/TiO_2/RGO aerogel for simultaneous water evaporation and purification. The hydrophilic Al_2O_3/TiO_2 fibrous channels pumped continuous water to RGO hot spots. Besides, Al_2O_3/TiO_2 nanofiber frameworks effectively hampered the stacking among RGO sheets, resulted in low density ($0.08\ g \cdot cm^{-3}$) of aerogel, enlarged light adsorption area and boosted thermal conduction within RGO sheets. Meanwhile, the Al_2O_3/TiO_2 nanofiber channels with thermal insulation effect powerfully stored the heat converted from RGO with bulky water insulation. This effective interfacial evaporation of Al_2O_3/TiO_2/RGO led to a 36% improvement in solar-to-vapor conversion efficiency (78.2%) compared to RGO aerogel (57.5%). Moreover, Al_2O_3/TiO_2 nanofibers effectively photodegraded pollutants into nontoxic molecules with a high dye removal ratio of 91.3%, achieving exciting synchronized solar-driven water evaporation and purification. Our work of advanced Al_2O_3/TiO_2 nanofibers overcame obstacles in conventional 3D photothermal aerogels and provided one-step approach for collecting clean water only driven by renewable solar energy.

Acknowledgements This work was financially supported by the National Natural Science Foundation of China (21975042), Natural Science Foundation of Jiangsu Province (BK20171153), the Project of Six Talents Climax Foundation of Jiangsu (XCL-082), the Equipment Pre-research Fund of National Defence Science and Technology Key Laboratory (614220504030817), the Fundamental Research Funds for the Central Universities, and the Priority Academic Program Development of Jiangsu Higher Education Institutions.

References

1. Cao S, Jiang Q, Wu X, Ghim D, Gholami H, Chou I, Jun S, Singamaneni S. Advances in solar evaporator materials for freshwater generation. *J Mater Chem A*. **2019**;*7*:24092.
2. Qtaishat R, Banat F. Desalination by solar powered membrane distillation systems. *Desalination*. **2013**;*308*:186.
3. Al-Karaghouli A, Kazmerski L. Energy consumption and water production cost of conventional and renewable-energy-powered desalination processes. *Renew Sustain Energy Rev*. **2013**;*24*:343.
4. Martinez-Huitle CA, Brillas E. Decontamination of wastewaters containing synthetic organic dyes by electrochemical methods: a general review. *Appl Catal B*. **2009**;*87*:105.
5. Jiang Y, Wang N, Biswas P, Fortner D. Facile aerosol synthesis and characterization of ternary crumpled graphene-TiO_2-magnetite nanocomposites for advanced water treatment. *ACS Appl Mater Interface*. **2014**;*6*:11766.
6. Han X, Wang W, Zuo K, Chen L, Yuan L, Liang J, Li Q, Ajayan M, Zhao Y, Lou J. Bio-derived ultrathin membrane for solar driven water purification. *Nano Energy*. **2019**;*60*:567.
7. Qin D, Zhu J, Chen F, Yang L, Xiong C. Self-floating aerogel composed of carbon nanotubes and ultralong hydroxyapatite nanowires for highly efficient solar energy-assisted water purification. *Carbon*. **2019**;*150*:233.
8. Cai T, Song J, Liu Y, Yin X, Li R, Yu Y, Ding B. Soft BiOBr@TiO_2 nanofibrous membranes with hierarchical heterostructures as efficient and recyclable visible-light photocatalysts. *Environ Sci Nano*. **2018**;*5*:2631.
9. Xue J, Wu T, Dai Y, Xia Y. Electrospinning and electrospun nanofibers: methods, materials, and applications. *Chem Rev*. **2019**;*119*:5298.
10. Li Z, Liu S, Song S, Xu W, Sun Y, Dai Y. Porous ceramic nanofibers as new catalysts toward heterogeneous reactions. *Compos Commun*. **2019**;*15*:168.
11. Wu X, Chen Y, Owens G, Chu D, Xu H. Photothermal materials: a key platform enabling highly efficient water evaporation driven by solar energy. *Mater Today Energy*. **2019**;*12*:277.
12. Shi Y, Li Y, Jin Y, Zhuo F, Shi L, Chang J, Hong S, Ng C, Wang P. A 3D photothermal structure toward improved energy efficiency in solar steam generation. *Joule*. **2018**;*2*:1171.
13. Chen C, Kuang Y, Hu L. Challenges and opportunities for solar evaporation. *Joule*. **2019**;*3*:683.
14. Gao M, Zhu L, Peh K, Ho W. Solar absorber material and system designs for photothermal water vaporization towards clean water and energy production. *Energy Environ Sci*. **2019**;*12*:841.
15. Dai Y, Sun Y, Yao J, Ling D, Wang Y, Long H, Wang X, Lin B, Zeng H, Sun Y. Graphene-wrapped TiO_2 nanofibers with effective interfacial coupling as ultrafast electron transfer bridges in novel photoanodes. *J Mater Chem A*. **2014**;*2*:1060.
16. Jiang F, Liu H, Li Y, Kuang D, Xu X, Chen J, Huang H, Jia C, Zhao P, Hitz E, Zhou B, Yang G, Cui F, Hu B. Lightweight, mesoporous, and highly absorptive all-nanofiber aerogel for efficient solar steam generation. *ACS Appl Mater Interfaces*. **2018**;*10*:1104.
17. Weng M, Zhou P, Chen L, Zhang L, Zhang W, Huang Z, Liu C, Fan S. Multiresponsive bidirectional bending actuators fabricated by a pencil-on-paper method. *Adv Funct Mater*. **2016**;*26*:7244.
18. Liu X, Cheng H, Guo Z, Zhan Q, Qian J, Wang X. Bifunctional, moth-eye-like nanostructured black titania nanocomposites for solar-driven clean water generation. *ACS Appl Mater Interface*. **2018**;*10*:39661.
19. Wang X, Zhu M, Sun Y, Fu W, Gu Q, Zhang C, Zhang Y, Dai Y, Sun Y. A new insight of the photothermal effect on the highly efficient visible-light-driven photocatalytic performance of novel-designed TiO_2 rambutan-like microspheres decorated by Au nanorods. *Part Part Syst Char*. **2016**;*33*:140.
20. Dai Y, Jing Y, Zeng J, Qi Q, Wang C, Goldfeld D, Xu C, Zheng Y, Sun Y. Nanocables composed of anatase nanofibers wrapped in UV-light reduced graphene oxide and their enhancement of photoinduced electron transfer in photoanodes. *J Mater Chem*. **2011**;*21*:18174.
21. Xu X, Zhang Q, Hao M, Hu Y, Lin Z, Peng L, Wang T, Ren X, Wang C, Zhao Z, Wan C, Fei H, Wang L, Zhu J, Sun H, Chen W, Du T, Deng B, Cheng G, Shakir I, Dames C, Fisher T, Zhang X, Li H, Huang Y, Duan X. Double-negative-index ceramic aerogels for thermal superinsulation. *Science*. **2019**;*363*:723.
22. Fu Y, Wang G, Mei T, Li J, Wang J, Wang X. Accessible graphene aerogel for efficiently harvesting solar energy. *ACS Sustain Chem Eng*. **2017**;*5*:4665.

23. Yang Y, Zhao R, Zhang T, Zhao K, Xiao P, Ma Y, Ajayan P, Shi G, Chen Y. Graphene-based standalone solar energy converter for water desalination and purification. *ACS Nano*. **2018**;*12*:829.
24. Gong F, Li H, Wang W, Huang J, Xia D, Liao J, Wu M, Papavassiliou D. Scalable, eco-friendly and ultrafast solar steam generators based on one-step melamine-derived carbon sponges toward water purification. *Nano Energy*. **2019**;*58*:322.
25. Fu W, Dai Y, Tian J, Huang C, Liu Z, Liu K, Yin L, Huang F, Lu Y, Sun Y. In situ growth of hierarchical Al_2O_3 nanostructures onto TiO_2 nanofibers surface: super-hydrophilicity, efficient oil/water separation and dye-removal. *Nanotechnology*. **2018**;*29*:345607.
26. Zhu B, Kou H, Liu Z, Wang Z, Macharia D, Zhu M, Wu B, Liu X, Chen Z. Flexible and washable CNT-embedded PAN nonwoven fabrics for solar-enabled evaporation and desalination of seawater. *ACS Appl Mater Interfaces*. **2019**;*11*:35005.
27. Liu Z, Wu B, Zhu B, Chen Z, Zhu M, Liu X. Continuously producing watersteam and concentrated brine from seawater by hanging photothermal fabrics under sunlight. *Adv Funct Mater*. **2019**;*29*:1905485.
28. Li X, Li J, Lu J, Xu N, Chen C, Min X, Zhu B, Li H, Zhou L, Zhu S, Zhang T, Zhu J. Enhancement of interfacial solar vapor generation by environmental energy. *Joule*. **2018**;*2*:1331.
29. Chen C, Li Y, Song J, Yang Z, Kuang Y, Hitz E, Jia C, Gong A, Jiang F, Zhu J, Yang B, Xie J, Hu L. Highly flexible and efficient solar steam generation device. *Adv Mater*. **2017**;*29*:1701756.
30. Wang G, Fu Y, Guo A, Mei T, Wang J, Li J, Wang X. Reduced graphene oxide-polyurethane nanocomposite foam as a reusable photoreceiver for efficient solar steam generation. *Chem Mater*. **2017**;*29*:5629.
31. Zha J, Zhao X, Pu H, Tang S, Ke K, Bao Y, Bai L, Liu Y, Yang B, Yang W. Flexible anti-biofouling mxene/cellulose fibrous membrane for sustainable solar-driven water purification. *ACS Appl Mater Interface*. **2019**;*11*:36589.
32. He Z, Yang S, Ju Y, Sun C. Microwave photocatalytic degradation of Rhodamine B using TiO_2 supported on activated carbon: mechanism implication. *J Environ Sci*. **2009**;*21*:268.
33. Li F, Lu C, Xu B, Cheng L. Photocatalytic degradation of Rhodamine B under visible light irradiation by TiO_2 doped layered zirconium phosphates. *J Nanosci Nanotechnol*. **2020**;*20*:1697.
34. Li Y, Chen W. Photocatalytic degradation of Rhodamine B using nanocrystalline TiO_2–zeolite surface composite catalysts: effects of photocatalytic condition on degradation efficiency. *Catal Sci Technol.* **2011**;*1*:802.

Xiangyu Meng is currently a PhD candidate in School of Chemistry and Chemical Engineering in Southeast University. She received the bachelor degree from Donghua University in 2017. Her current research interests include graphene-based materials and electrospun nanofibers.

Wanlin Xu is a master student in School of Chemistry and Chemical Engineering in Southeast University since 2019. She received the bachelor degree from Southeast University in 2019. Her current research is electrospun ceramic nanofibers.

Zhihui Li is a master student in School of Chemistry and Chemical Engineering in Southeast University since 2018. She received the bachelor degree from Wuhan University of Technology in 2018. Her current research is exploring porous nanofibers toward heterogeneous catalysis.

Jianhui Yang is currently a undergraduate student in School of Chemistry and Chemical Engineering in Southeast University. His current research project is fabricating novel carbon-based nanomaterials.

Jingwu Zhao was a undergraduate student School of Chemistry and Chemical Engineering in Southeast University and obtained bachelor degree in 2019.

Xixi Zou was a undergraduate student School of Chemistry and Chemical Engineering in Southeast University and obtained bachelor degree in 2019.

Yueming Sun received a PhD degree in coordination chemistry from Nanjing University in 1991. He is the professor in School of Chemistry and Chemical Engineering at Southeast University. His research interests include dye molecular engineering, theoretical and computational chemistry, design and synthesis novel nano-electrodes and electrolytes for applications in solar cells, batteries, and fuel cells.

Yunqian Dai received her Ph.D. in Materials Physics and Chemistry from Southeast University in 2011. She spent two years as a visiting graduate student at Washington University in St. Louis from 2008 to 2010. She started as an Assistant Professor in the School of Chemistry and Chemical Engineering in Southeast University in 2011 and then promoted to Professor in 2019. Her current research interests include electrospun nanofibers, carbon-based nanomaterials, and their applications in catalysis, environmental science, and energy technology.